



Factors Affecting Reaction Jet Interaction Effects on Projectiles

James DeSpirito¹

U.S. Army Research Laboratory, Aberdeen Proving Ground, Maryland, 21005

The flow interaction effects from a jet issuing into a supersonic crossflow were investigated computationally for the case of a flat plate and a generic fin-stabilized projectile. For both configurations, simulations were performed at several Mach numbers and jet total to freestream static pressure ratios (PR). Several additional parameters were investigated using the flat plate configuration, e.g., nozzle exit to throat area ratio, jet total temperature, and freestream altitude. In the flat plate case, the jet force was generally amplified, with a strong dependence on PR and the freestream Mach number. In the projectile configuration, the jet force was generally attenuated, unless the jet was located very close to the tail fins. In the latter case, this results from a combination of little or no projectile surface area for the detrimental jet interaction effects to act on and the high pressures developed on the fin surfaces. The choice of turbulence model was found to be an important parameter, making the availability of experimental validation data is important.

Nomenclature

ANF	=	Army-Navy Finner projectile
AR	=	jet exit area to throat area ratio
C_{Nji}	=	jet interaction force coefficient
c.g.	=	projectile center of gravity, m or caliber
C_{Nj}	=	jet thrust force coefficient
C_{mji}	=	pitching moment coefficient due to jet interaction force
C_{mj}	=	pitching moment coefficient due to jet thrust force
d	=	projectile diameter, m
F_{ji}	=	jet interaction force, N
F_j	=	jet thrust force, N
F_{total}	=	total normal force (thrust + interaction), N
F_{no-jet}	=	normal force without jet, N
J	=	jet exit to freestream dynamic pressure ratio
K_f	=	jet force amplification factor
K_m	=	jet moment amplification factor
M	=	Mach number
M_{ji}	=	moment induced by jet interaction force, N-m
M_j	=	moment induced by jet thrust force, N-m
M_{total}	=	moment induced by total normal force, N-m
p_∞	=	freestream static pressure, Pa
p_0	=	freestream total pressure, Pa
p_{0j}	=	jet total pressure, Pa
PR	=	jet total to freestream static pressure ratio, p_{0j} / p_∞
PR ₀	=	jet total to freestream total pressure ratio, $p_{0j} / p_{0\infty}$
STP	=	Standard temperature and pressure
T_∞	=	freestream static temperature, K
T_0	=	freestream total temperature, K

¹ Aerospace Engineer, Flight Science Branch, RDRL-WML-E, AIAA Associate Fellow.

T_{0j} = jet total temperature, K
 x_{cp} = force center of pressure

I. Introduction

The study of jets issuing into a crossflow has been the subject of research for about seventy years.¹⁻³ The primary purpose of such a reaction jet control (RJC) system is to generate a lateral force or moment to provide attitude or roll control for a flight vehicle. There are several advantages of RJC systems over conventional aerodynamic controls such as canards or fins, e.g., increased maneuver authority when operating in low dynamic pressure (low velocity or high altitude), small time delay for the actuation effect, and compact design. In addition, the external aerodynamics of the flight vehicle is unaffected except during the actuation period of the jet. The main disadvantage of a RJC system is the effect of the jet interaction (JI) flowfield on the control forces and moments. Research shows the operation of a lateral reaction jet in atmospheric flight results in an interference flow between the jet plume and the flow over the vehicle.^{2,3} The JI effect increases the difficulty of determining simple models of RJC systems to apply the technology.⁴

The study of reaction jet interaction effects is still an active area of research. Some recent computational studies include the shock-boundary layer interaction effects on a flat plate⁵ and a body of revolution,⁶ and experimental and computation results on a flat plate⁷ and generic missile configurations.⁸⁻¹¹ Experimental studies including particle image velocimetry (PIV) measurements on a flat plate¹²⁻¹⁴ and a missile configuration^{15,16} provide valuable information on the flowfield structure away from the body surfaces.

The currently accepted flow structure in the near field of a supersonic jet issuing into a supersonic crossflow is illustrated in Fig. 1, as presented by Champigny and Lacau³ for a flow over a flat plate. One of the main features is due to the jet stream acting as an obstruction to the flow. A shock-boundary layer interaction forms upstream of the jet as the approaching boundary layer interacts with the bow shock, leading to a λ -shock structure. The separated flow in this region wraps around the jet and forms the counter-rotating horseshoe vortices that stay near the wall surface. The jet plume is curved in the direction of the flow due to the freestream crossflow. A "barrel" shock surrounds the jet plume and terminates in a Mach disk. Two counter-rotating wake vortices form and travel downstream as the primary flow feature of the jet plume. These vortices likely originate from the ring vortices of the jet shear layer as they exit the orifice, which get transformed as they interact with the crossflow.³

The flow structure in the near field of a supersonic jet issuing from a body of revolution, i.e., a projectile or missile, is similar to that for the flat plate and is shown in Fig. 2 (from Ref. 10). Some differences are that the jet is now located behind the bow shock formed at the nose of the projectile. Also, the jet bow shock and horseshoe vortices emanating from the separation region will tend to "wrap-around" the projectile body. The basic features of the separation region and λ -shock are very similar to that observed with a jet issuing from a flat plate. A strong turbulent wake extends behind the jet and a recompression shock forms downstream.

Accurate prediction of the JI effects is important for predicting the overall forces and moments imparted to the projectile, as the presence of the lateral jet will affect the entire flowfield. The flow disturbances due to the JI will

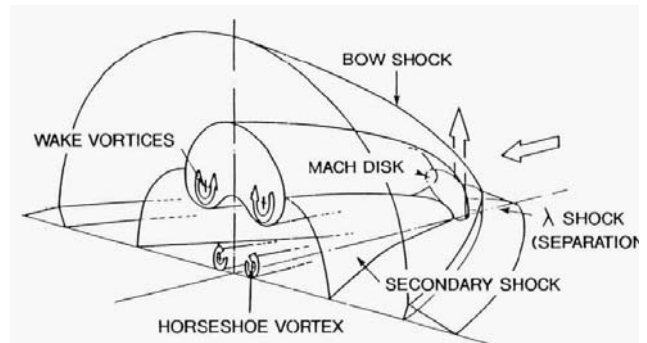


Figure 1. Accepted flow structure of jet injecting into a supersonic crossflow from a flat plate.³

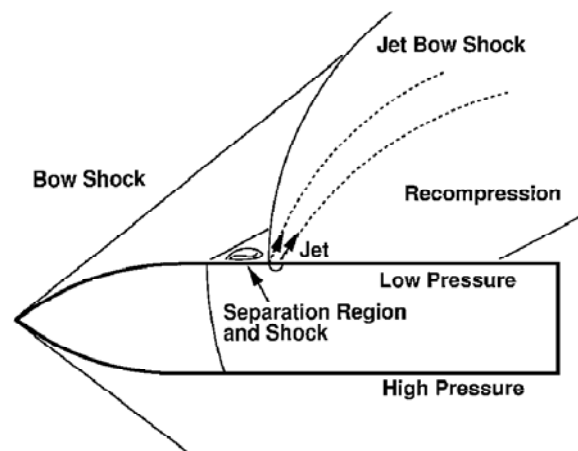


Figure 2. Schematic of a jet interaction flowfield around a body of revolution.¹⁰

alter the forces and moments that would otherwise be expected to be produced from the jet thrust alone. Since a high pressure region is produced ahead of the jet and a low pressure region produced behind the jet, a net moment is also produced (typically nose down for the configuration shown in Fig. 2). The part of the jet bow shock that wraps around the projectile body increases the pressure underneath the projectile, adding to that induced moment. The overall effect is that both the control force and moment produced by the lateral jet may be augmented or attenuated due to JI effects.

The objective of the present study is to investigate some parameters affecting the control forces and moments of a lateral reaction jet acting on a generic, fin-stabilized (finner) projectile. The present study focuses on a supersonic crossflow, while a future investigation will explore the subsonic and transonic flight regimes. Parameters investigated were the jet total pressure to freestream static pressure ratio (PR), the nozzle exit to throat area ratio (AR), and the jet location on the projectile. An archival flat plate experimental study¹⁷ was used as a validation case and to compare the jet interaction flowfield over a flat plate with that of a body of revolution. In addition to the above mentioned parameters, the jet gas total temperature, T_{0j} , was also evaluated in the flat plate study. The performance of several turbulence models were also evaluated in the flat plate configuration.

II. Numerical Approach

A. Flat Plate Model

Several of the flat plate experiments of Dowdy and Newton¹⁷ were used as validation cases and for comparison of the jet interaction effects with that of a body of revolution. The experiment used a 457.2 mm long by 444.5 mm wide flat plate, while the simulations use a square plate with 457.2 mm to a side. Figure 3 shows the computational model of the setup including the mesh on the boundary surfaces. Using the symmetry of the setup, only one-half of the domain was modeled. A cylindrical, sonic jet orifice was located 177.8 mm from the leading edge, on the centerline of the plate. The nozzle is shown in Figs. 3c and 3d. The jet orifice diameter was 2.54 mm (0.1") and the length was 1.6 mm, which was about 1 mm shorter than that in the actual experimental setup. The geometry of the plenum was also modified from that of the actual experiments; a diameter of 10 mm vs. 8.9 mm in the experiment, and a longer convergent section. The simulation of the jet has been found to be relatively insensitive to the length of the plenum, as long it is long enough to warrant a stagnation boundary condition at the far end.

The computational domain was bounded by the flat plate on the lower end, the plate edges, and a top surface that is 178 mm above the plate surface. The boundary conditions were set as a no-slip wall surface on the plate and supersonic freestream conditions (a characteristics-based inflow/outflow based on solving a Riemann problem at the boundary) on the other five boundary surfaces. The inlet to the nozzle plenum was modeled as a subsonic reservoir boundary inflow with a specified total temperature and pressure. This is a preferred method of directly modeling the nozzle geometry, rather than imposing a boundary condition at the jet exit. There is only a relatively small cost in increased mesh size.

The computational domain was meshed with the MIME grid generator from Metacomp Technologies.¹⁸ The mesh consisted of tetrahedral cells with triangular prism layers projected from the solid wall surfaces, including the nozzle plenum and throat. Density boxes (shown in Fig. 3) were used to refine the grid in regions where large flow gradients are expected. A mesh resolution study was performed using meshes of 4.08, 10.5, and 19.0 M cells and results are presented in Section III-A-1. The mesh was refined primarily in the density box that contained the jet and the resulting interaction region (the larger box shown fully in Figs. 3b and 3c). The baseline mesh for the validation study was the 4.08 M mesh. The first cell wall spacing was 0.001 mm, leading to final y^+ values less than one on the plate surface, as the "solve-to-wall" methodology was used. The plenum and nozzle exit walls were modeled with an advanced two-layer wall function boundary condition that reverts to a solve-to-wall method where the mesh is fine enough; or else to a wall function, as on the nozzle walls. This was necessary as the flow conditions changed significantly in the throat and nozzle exit region and the y^+ values approach 100 in that region with the current wall adjacent cell spacing.

The wind tunnel test flow conditions for selected tests are summarized in Table 1. The jet total to freestream static pressure ratio, PR, is listed for each case. The jet total to freestream total pressure ratio, PR_0 , and the jet to freestream dynamic pressure, J , are also listed, as these parameters can also be used to define the strength of the jet. Both the jet and the freestream are modeled as air using ideal gas assumptions. A nitrogen jet was used in the experiment, but it is assumed the effects of simulating this with an air jet are minimal. No force measurements were made in the experimental investigation, so comparisons of surface pressure traces are the primary validation criteria. A comparison of turbulence models was also performed with this configuration and results are presented in Section III-A-2.

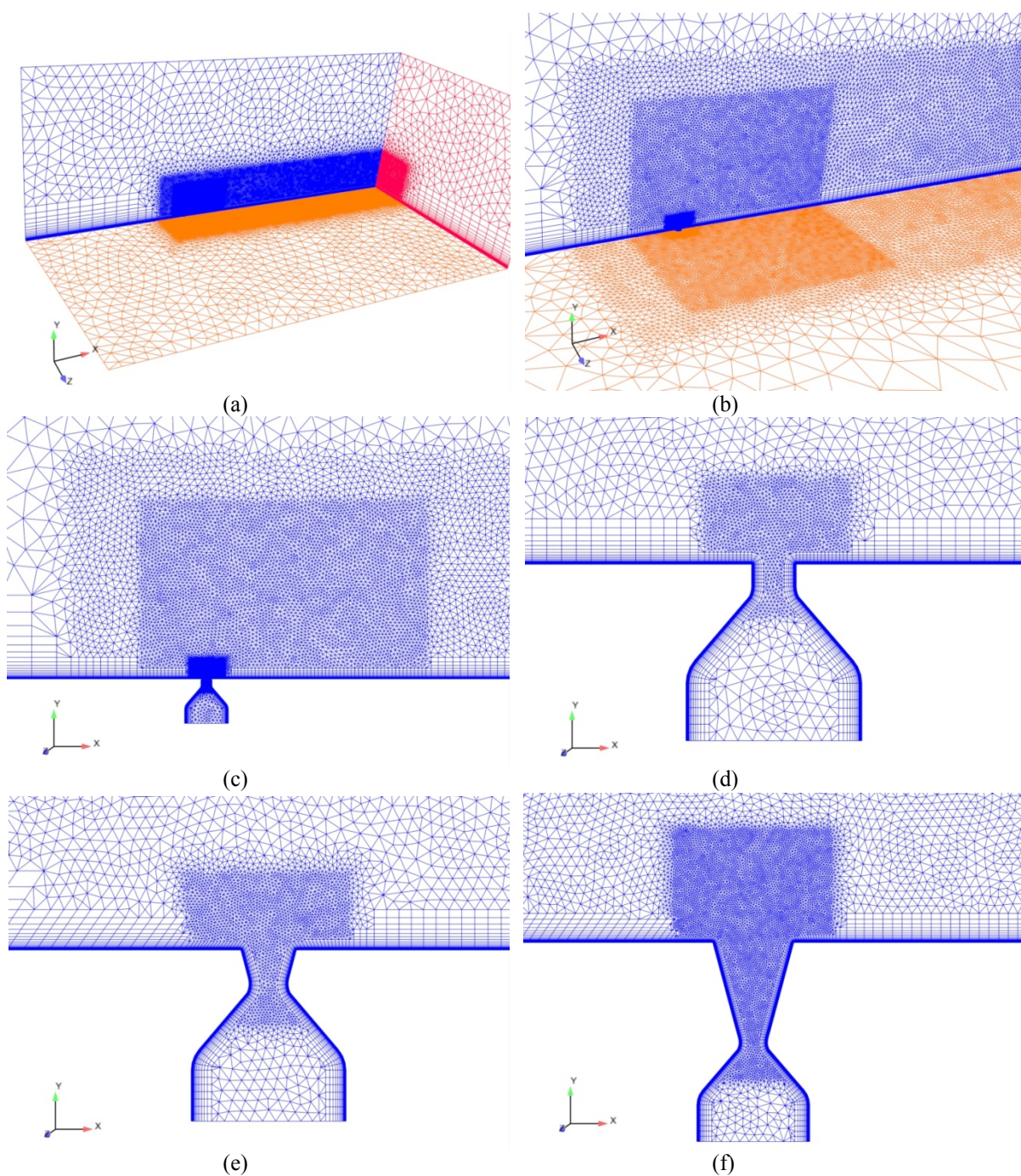


Figure 3. Geometry and mesh used for flat plate simulations: (a-c) density boxes within computational domain, (d) sonic (AR=1) nozzle, (e) AR=2 nozzle, and (f) AR=8 nozzle.

Table 1. Flow conditions of flat plate validation simulations.

Run No.	M	p_{0j} (Pa)	T_{0j} (K)	p_{∞} (Pa)	T_{∞} (K)	PR	PR_0	J
30-5	2.01	1.418×10^6	296.48	18767.5	131.2	75.5	9.62	9.88
26-6	2.61	2.069×10^6	296.48	6729.1	132.8	307.5	15.4	23.9
24-4	3.50	3.130×10^5	296.48	1344.5	129.8	232.8	3.02	10.0
19-2	4.54	3.702×10^5	297.59	1165.2	134.3	317.8	0.99	8.15

A nozzle parameter study was also conducted with this same computational setup. The parameters of this study are shown in Table 2, which are all for a sonic jet configuration. Most simulations were performed at STP freestream conditions (101,325 Pa and 288 K) and with a cold jet, $T_0 = 300$ K. Simulations were also performed with two hot jets, $T_0 = 1500$ and 2700 K; and at freestream conditions equivalent to altitudes of 2 km and 10 km, which primarily increases the pressure ratios. Three jet total pressures were investigated: 34.5, 15.0, and 5.0 MPa, representing a highly energetic gas jet, a moderately energetic gas jet, and a pressurized inert gas typical of a laboratory setup, respectively.

Two additional nozzles (Fig. 3e, and 3f), with $AR=2$ and $AR=8$, were also investigated at Mach 2.5 and STP conditions. For these nozzles, PR and PR_0 are the same as that for the sonic nozzle listed in Table 2. However, J is different due to the modified jet velocity and density at the exit. The dynamic pressure ratio was observed to decrease with increasing AR , as the density at the jet exit decreases more significantly than the jet velocity increases. The plenum and throat geometry were constant for the three nozzles.

Table 2. Flow conditions used in flat plate nozzle parameter study (sonic jet).

Flow Conditions	M	p_{0j} (Pa)	T_{0j} (K)	p_{∞} (Pa)	T_{∞} (K)	PR	PR_0	J
STP	1.2	5.00×10^6	300.0	101325.	288.15	49.3	20.3	18.1
	1.2	1.50×10^6	300.0	101325.	288.15	148.0	61.0	54.3
	1.2	3.45×10^7	300.0	101325.	288.15	340.5	140.4	125.0
STP	1.7	5.00×10^6	300.0	101325.	288.15	49.3	10.0	9.02
	1.7	1.50×10^6	300.0	101325.	288.15	148.0	30.0	27.1
	1.7	3.45×10^7	300.0	101325.	288.15	340.5	69.0	62.3
STP	2.5	5.00×10^6	300.0	101325.	288.15	49.3	2.89	4.17
	2.5	1.50×10^6	300.0	101325.	288.15	148.0	8.66	12.5
	2.5	3.45×10^7	300.0	101325.	288.15	340.5	19.9	28.8
STP	2.5	5.00×10^6	1500.	101325.	288.15	49.3	2.89	4.17
	2.5	1.50×10^6	1500.	101325.	288.15	148.0	8.66	12.5
	2.5	3.45×10^7	1500.	101325.	288.15	340.5	19.9	28.8
STP	2.5	5.00×10^6	2700.	101325.	288.15	49.3	2.89	4.17
	2.5	1.50×10^6	2700.	101325.	288.15	148.0	8.66	12.5
	2.5	3.45×10^7	2700.	101325.	288.15	340.5	19.9	28.8
2 km	2.5	5.00×10^6	300.0	79494.	275.15	62.9	3.68	4.56
	2.5	1.50×10^6	300.0	79494.	275.15	188.7	11.0	13.7
	2.5	3.45×10^7	300.0	79494.	275.15	434.0	25.4	31.5
10 km	2.5	5.00×10^6	300.0	26436.	223.15	189.1	11.1	13.7
	2.5	1.50×10^6	300.0	26436.	223.15	567.4	33.2	41.2
	2.5	3.45×10^7	300.0	26436.	223.15	1305.	76.4	94.7

Downloaded by UNIV OF CALIFORNIA SAN DIEGO on February 9, 2016 | http://arc.aiaa.org | DOI: 10.2514/6.2011-3031

Table 3. Jet locations along Army-Navy Finner projectile.

The computational domain (Fig. 5) was designed relatively conservatively for supersonic flow, so one mesh could be used for low- to mid-supersonic Mach numbers. The forward edge of the domain starts 5 cal. in front of the projectile; the end of the domain is 20 cal. behind the projectile base; and the radial extent of the domain is 14.5 cal. from the projectile body surface. The computational domain was meshed with MIME.¹⁸ The mesh consisted of tetrahedral cells and triangular prism layers projected from the solid wall surfaces. Using the symmetry of the system, only a half model was meshed. The meshes on the symmetry plane and projectile surfaces are shown in Fig 5. Density boxes, which allow finer control of the mesh characteristics, are used to refine the mesh in expected regions of high gradients. Figures 5a-c show the density boxes used around the whole projectile, the wake, and in the J1 region. Two density boxes used for the J1 region were moved along the projectile as the jet location moved. Figure 5b shows the mesh for the jet in the F0 location, while Figure 5c shows the mesh for the jet in the F2 location. As the jet location was moved rearward there was a small reduction in the required mesh size. The total mesh sizes ranged from 8.8 M cells for the jet in the R3 location to 10.2 M cells for the jet in the F3 location.

6

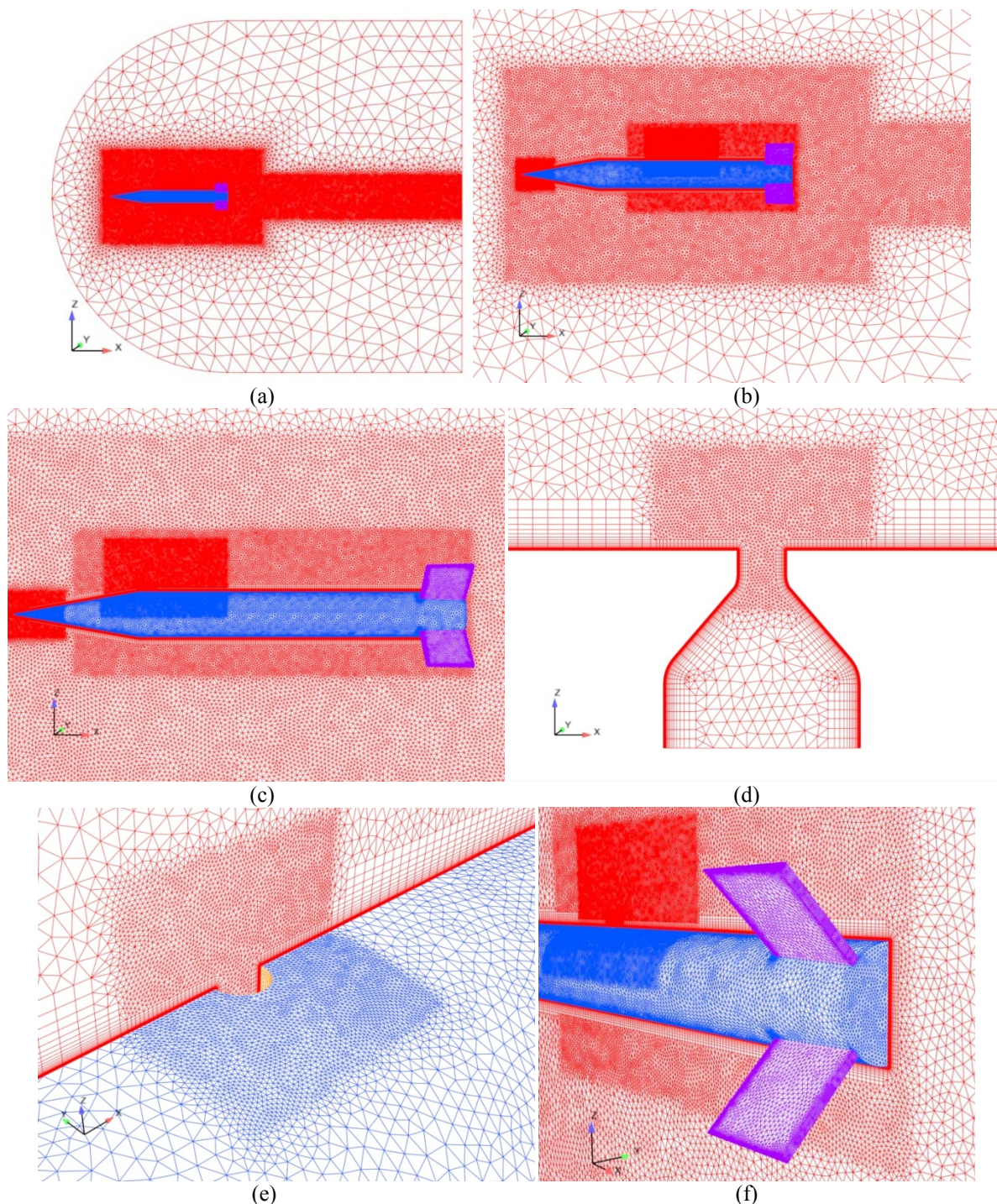


Figure 5. Geometry and mesh used for ANF simulations: (a) symmetry plane of computational domain, (b) density boxes for F0 jet location, (c) density boxes for F2 jet location, (d) sonic nozzle, (e) surface mesh near nozzle exit, and (f) surface meshes on projectile and symmetry plane.

Prism layers were used along all solid boundaries, including the nozzle plenum and throat. The projectile and fin surfaces were modeled with the “solve-to-wall” methodology. The first cell wall spacing was 0.001 mm, resulting in y^+ values less than 1.0 everywhere except in the interaction region directly in front of the jet, where the values were still less than 2.0. The y^+ values were found to be between 50 and 100 on the nozzle exit walls, due to the

different flow properties from the gas expansion there. Therefore, the plenum and nozzle exit walls were modeled with an advanced two-layer wall function boundary condition that reverts to a solve-to-wall method where the mesh is fine enough; or else to a wall function, as on the nozzle walls.

The freestream conditions were based on standard sea level conditions: a static pressure of 101325 Pa and a static temperature of 288 K for Mach 2.5 (850.7 m/s) and Mach 1.5 (510.4 m/s) flows. Three jet total pressures were investigated: 34.5, 15.0, and 5.0 MPa, giving PR values of 340, 148, and 49, respectively. The jet total temperature was 2700 K for all cases.

C. Computational Details

The commercially available CFD++ code,²¹ version 10.1, was used in this study. The 3-D, compressible, Reynolds-averaged Navier-Stokes (RANS) equations are solved using a finite volume method. A point-implicit time integration scheme with local time-stepping, defined by the CFL (Courant-Friedrichs-Lewy) number, was used to advance the solution towards steady-state. The multigrid W-cycle method with a maximum of 4 cycles and a maximum of 20 grid levels was used to accelerate convergence. Implicit temporal smoothing was applied for increased stability, which is especially useful where strong transients arise. The inviscid flux function was a second-order, upwind scheme using a Harten-Lax-van Leer-Contact (HLLC) Riemann solver and a multi-dimensional Total-Variation-Diminishing (TVD) continuous flux limiter.²¹

The choice of turbulence model is a key factor in the numerical modeling of complex flows such this, and CFD++ has a large set of turbulence models available. For this study, the two-equation Menter's Shear Stress Transport (SST) model²² was chosen based on some previous experience with shock-boundary layer interaction (SBLI) flows. However, as will be shown in Section III-A-2, similar to observations for SBLI flows,²³ no single turbulence model has been shown to accurately predict all aspects of the jet interaction phenomena.

The CFL number was typically ramped from 0.1 to about 20 or 40 (depending on Mach number and PR) over the first 200 iterations, and remained at that level until convergence. Although CFL numbers up to 40 are typically used in CFD++ for the freestream Mach numbers used in this study, the Mach number in the jet is much higher and the CFL numbers used are more typical of that used in hypersonic flow, leading to more stable convergence. Convergence was determined by a 5-6 order decrease in the magnitude of the maximum residuals and ensuring that the integrated forces and moments on the projectile were not changing with increased iterations. The mass and energy flux through the jet orifice was also tracked and usually converged before the projectile forces and moments. Typically, 2400 to 4800 iterations were required to converge to steady state solutions. The mesh was partitioned with approximately 150,000 to 200,000 cells per CPU core, usually 48 to 72 computing cores, depending on the configuration. Simulations were performed on a SGI Altix ICE 8200 Supercomputer (HAROLD) and a Linux Networx Advanced Technology Cluster (MJM) at the Army Research Laboratory DoD Supercomputing Resource Center (DSRC) at Aberdeen Proving Ground, MD, and a Cray XE6 (RAPTOR) at the Air Force Research Laboratory DSRC at Wright-Patterson Air Force Base, OH.

III. Results and Discussion

It has become common practice to define the net control force and moment produced by the JI in terms of an "amplification factor." These jet force and moment amplification factors are defined as

$$K_f = \frac{F_j + F_{ji}}{F_j} = \frac{C_{N_j} + C_{N_{ji}}}{C_{N_j}} \quad (1)$$

and

$$K_m = \frac{M_j + M_{ji}}{M_j} = \frac{C_{m_j} + C_{m_{ji}}}{C_{m_j}}. \quad (2)$$

An amplification factor greater than one indicates the JI effect increases the effectiveness of the jet thrust force, F_j , or the moment induced by the jet thrust, M_j . In the literature (e.g. Ref. 4), the jet "vacuum" thrust is sometimes used in the denominator of Eq. (1). Here the actual jet thrust is used, which is measured on a plane at the nozzle exit. CFD++ outputs the forces (and fluxes) on this defined plane, as it does for any other boundary.

The total force on the body is the sum of the jet thrust force, the force due to the JI, and the force due to the angle of attack of the body with respect to the freestream without the jet. Therefore, the force due to the JI can be determined from Eq. 3,

$$F_{ji} = F_{\text{total}} - F_{\text{no-jet}} - F_j, \quad (3)$$

where F_{total} is total force due to the jet thrust, JI effects, and angle of attack. $F_{\text{no-jet}}$ is the force in the absence of the jet, which will be non-zero at non-zero α . Moments due to these forces follow directly and the equations using coefficients are similar. On a flat plate or a projectile at zero angle of attack, the JI force and moment are computed directly, since there is no force normal to the surface with the jet off.

If moments are referenced from the center of gravity, c.g., the interaction center of pressure location, measured from the c.g., are calculated from

$$x_{\text{cp}_{\text{total}}} = \frac{-M_{\text{total}}}{F_{\text{total}}}, \quad x_{\text{cp}_j} = \frac{-M_j}{F_j}, \quad x_{\text{cp}_{ji}} = \frac{-M_{ji}}{F_{ji}}, \quad (4)$$

for the “total,” “jet thrust,” and “interaction” forces, respectively. A positive x_{cp} indicates a location to the rear of the c.g., while a negative x_{cp} indicates a location forward of the c.g. A nose-down or nose-up rotation about the c.g. depends on the sign of the moment, with a negative moment indicating a nose-down rotation.

A. Flat Plate Case.

1. Grid Resolution Study

A grid resolution study was performed using the SST turbulence model and the conditions of the Run No. 26-6 case from Table 1 (Mach 2.61). The baseline (4.08 M cell) mesh and two finer meshes of 10.5 and 19.0 M cells were investigated. The first cell spacing and spacing ratio in the prism layer were kept constant. In general, there is very little difference in the simulation data among the different meshes (Fig. 6). There is a difference very close to the jet exit in the lateral direction profile (Fig. 6b). However, there are no experimental data points this close to the jet. It was decided that the baseline, 4.08 M cell mesh was adequate for the purpose of this study. It is believed that a mesh adaption capability would be advantageous in these jet interaction type simulations. This capability is planned for the next version of CFD++ and will be applied in future simulations.

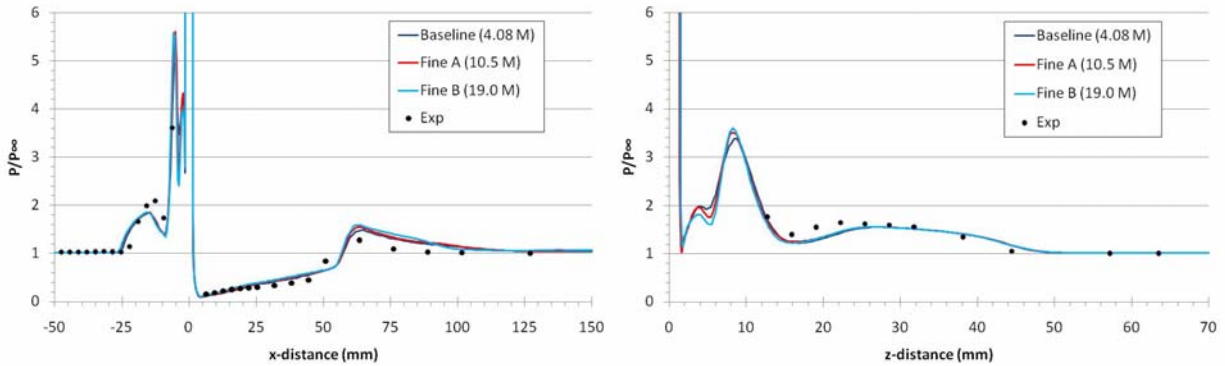


Figure 6. Comparison of normalized pressure profiles on flat plate for Run No. 26-6 (Mach 2.61).¹⁷

2. Turbulence Model Study

Simulations were also performed comparing six turbulence models for each of the four cases in Table 1. The models used were the (i) Menter’s Shear Stress Transport (SST) 2-equation model,²² (ii) Spalart-Allmaras’s (SA) 1-equation model,²⁴ (iii) the Realizable k- ϵ (RKE) 2-equation model,²⁵ (iv) the cubic k- ϵ (CKE) non-linear, 2-equation model,²⁶ (v) Goldberg’s R_t (RT) 1-equation model,²⁶ (vi) Goldberg’s k- ϵ -R (KER) 3-equation model,²⁷ and the (vii) Reynolds Stress Transport (RSM) 2nd moment closure, 7-equation model.²⁸ These results are shown in Fig. 7, where profiles are shown along the plate centerline forward and rearward of the jet (left side of figure), and laterally to the side of the jet (right side of figure).

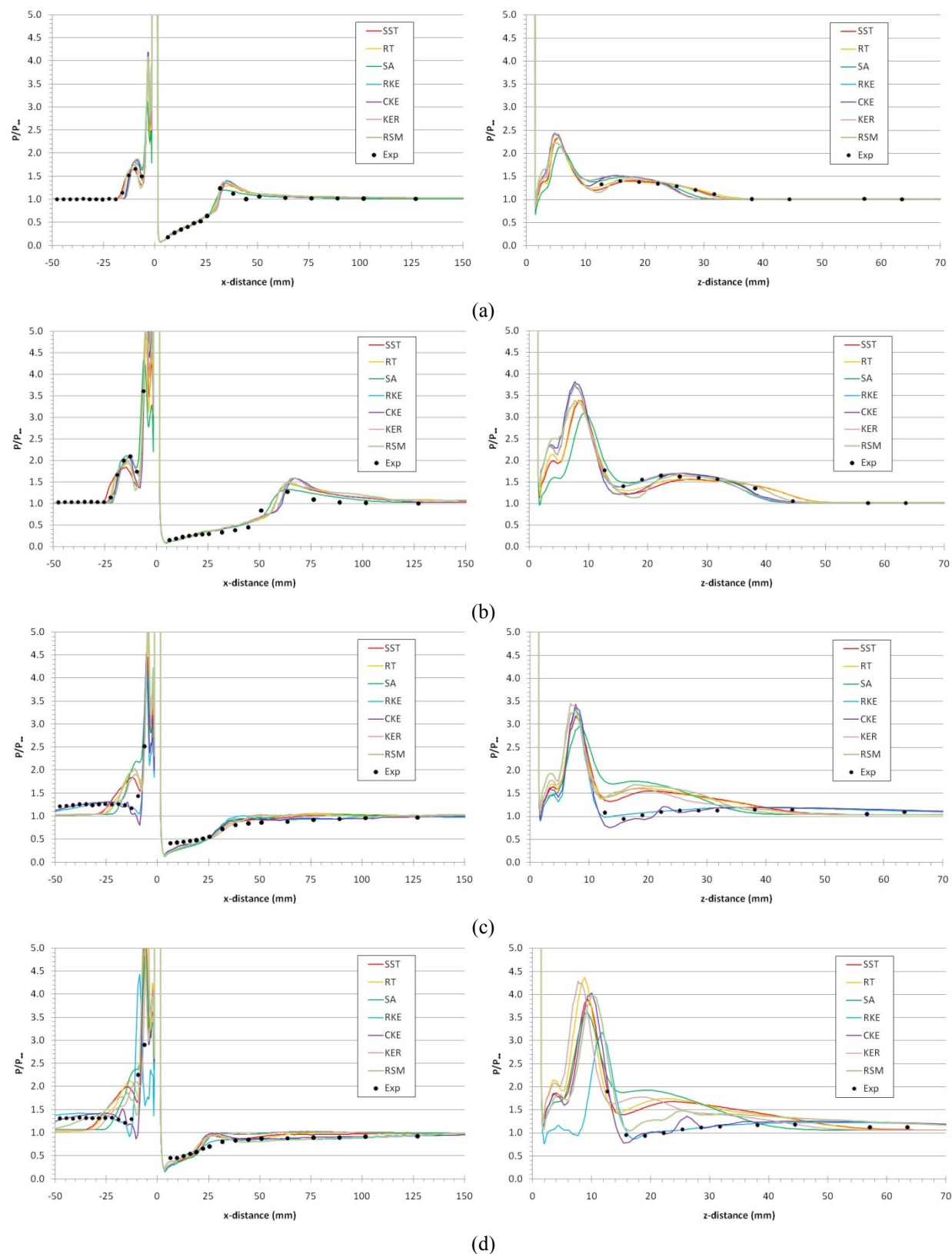


Figure 7. Comparison of normalized pressure profiles on flat plate, (left) forward and rearward of jet and (right) laterally from jet (a) Run 30-5 (Mach 2.01), (b) Run 26-6 (Mach 2.61), (c) Run 24-4 (Mach 3.5), and (d) Run 19-2 (Mach 4.54).

The results are somewhat inconclusive, as different models perform better in different parts of the flow and different crossflow Mach numbers (Fig. 7). At Mach 2.01 (Run 30-5, Fig. 7a), all models perform reasonably ahead of the jet, though the SST, RT, and RSM models slightly better predict the boundary layer separation point. All models also perform adequately in capturing pressure profile behind the jet, with the SA model not over predicting the maximum pressure rise. In the direction laterally from the jet, again the SST, RT, and RSM models more accurately predict the pressure profile. It follows that the accurate prediction of the features ahead of the jet will lead to more accurate prediction of the lateral pressure profile, as those features “wrap-around” to the side of the jet (e.g., see Fig. 1). At Mach 2.61 (Run 26-6, Fig. 7b), the SA model appears to perform the best, while the SST model is the least accurate in predicting the pressure profile ahead of the jet. The RSM model appears to predict the pressure profiles the best in this case. At Mach 3.5 and 4.54 (Run 24-4, Fig. 7c, and Run 19-2, Fig. 7d, respectively), The RKE and CKE models accurately predict the boundary layer separation ahead of the jet, while the other models lead to poor results (except the RSM model approaches the better prediction for the Mach 4.54 case (Fig. 7d). The predictions in the lateral direction again follow from how accurate the predictions are ahead of the jet.

It is believed that the meshes used in this study are adequate for the flows involved. In all cases the y^+ values were much less than 1.0, typically much less than 0.5 in the regions of interest in Fig. 7. All turbulence models were used with the default constants. A future investigation will attempt to address the turbulence model issue.

As the SST model was used as the primary turbulence model in the studies presented in this paper, an estimate of the potential error in the results is made by comparing the standard deviation of the jet force amplification factor, K_f , and the JI force, F_{ji} . Table 4 shows these results for each of the four cases, where the absolute values of the JI force is shown. The percent standard deviation was about 8–13% for K_f and about 10–16% for F_{ji} , indicating the potential level of error in the results to follow. However, since the primary investigations presented in this paper involve comparison of trends with varying jet parameters, valid conclusions can still be drawn from the results.

Table 4. Results from turbulence model study.

Turbulence Model	K_f	$ F_{ji} $	K_f	$ F_{ji} $	K_f	$ F_{ji} $	K_f	$ F_{ji} $
	Run 30-5 ($M=2.01$)		Run 26-6 ($M=2.61$)		Run 24-4 ($M=3.5$)		Run 19-2 ($M=4.54$)	
SST	4.79	33.2	3.46	31.8	7.23	12.1	9.19	18.9
RT	5.21	36.7	3.66	34.3	7.42	12.5	9.03	18.5
SA	4.95	34.5	3.53	32.7	7.49	12.6	9.59	19.8
RKE	4.40	29.8	3.10	27.2	5.46	8.7	7.21	14.3
CKE	4.27	28.7	3.03	26.3	5.87	9.5	8.07	16.3
KER	4.46	30.3	3.20	28.5	6.26	10.2	9.30	19.1
RSM	5.26	37.2	3.69	34.7	7.80	13.2	9.38	19.3
Average	4.76	32.9	3.38	30.8	6.79	11.2	8.82	18.0
Std. Dev.	0.40	3.4	0.27	3.4	0.91	1.8	0.86	2.0
% Std. Dev.	8.35	10.4	7.94	11.2	13.4	15.7	9.8	11.0

3. Nozzle Parameter Study

The nozzle parameter study (Table 2) was performed with the same computational domain and mesh. The flowfield for the Mach 1.7 and 2.5 cases are shown in Fig. 8. The contours of Mach number on the symmetry plane show several key features of the flow sketched in Fig. 1. The λ -shock separation zone is observed ahead of the bow shock and the barrel shock and Mach disk are clearly observed. The Mach disk is more clearly defined in the Mach 1.7 freestream (Fig. 8a) and the overall size of the barrel shock is larger than in the Mach 2.5 freestream flow. Although the pressure profiles in Fig. 6 are for different conditions (Mach 2.61), the features can be qualitatively compared to the pressure contours observed in Fig. 8b, for the Mach 2.5 flow. In both figures, along the symmetry plane, one can see the pressure rise in the boundary layer separation region (behind the λ -shock and ahead of the jet bow shock), followed by a decrease in pressure and then the large increase in pressure behind the jet bow shock. Behind the jet, there is a large region of low pressure, followed by small increase above the freestream pressure, and

then a gradual reduction to equilibration of the surface pressure with that of the freestream. Laterally from the jet, one sees that the first pressure peak in Fig. 7b is due to crossing the bow shock and the second, lower peak is due to crossing the weaker λ -shock.

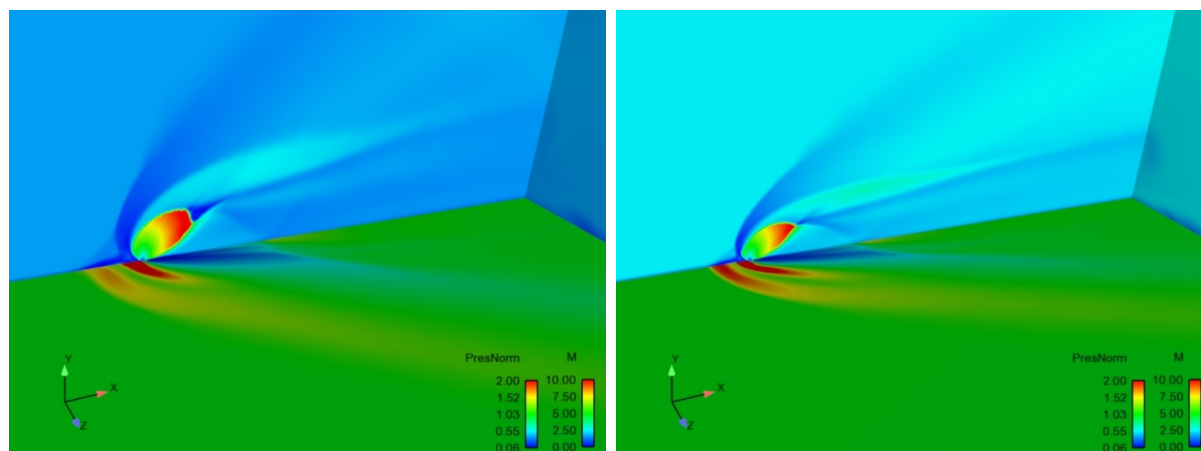


Figure 8. Flow field around flat plate at (a) Mach 1.7 and (b) Mach 2.5. Shown are Mach number contours on symmetry and far field planes and normalized pressure contours on plate surface.

The results of this study are shown in Tables 5–7. Table 5 shows the results for three Mach numbers, three pressure ratios, and three nozzle area ratios performed at STP freestream conditions and $T_{0j}=300$ K. Table 6 expands the study to include two more jet total temperatures, 1500 and 2700 K, at Mach 2.5 and with the sonic nozzle. Table 7 compares the JI effect at altitude by comparing a Mach 2.5 freestream flow at sea level (SL) with that at 2 km and 10 km in a standard atmosphere, all with an AR=2 nozzle and $T_{0j}=300$ K. Generally, the data show that the jet force is amplified ($K_f > 1$) for jets issuing into a supersonic freestream. The force amplification factor does decrease toward 1.0 as the freestream Mach number is decreased, and the Mach 1.2, PR=340 case shows attenuation of the jet force.

Table 5. Results from nozzle parameter study at STP freestream conditions ($T_{0j}=300$ K).

Mach No.	PR	K_f	K_m	F_{ji}	F_{total}	K_f	K_m	F_{ji}	F_{total}	K_f	K_m	F_{ji}	F_{total}
		AR=1				AR=2				AR=8			
1.2	340	0.83	-1.77	36.5	-180.	0.77	-1.56	56.3	-188.	0.72	-1.43	75.5	-196.
1.7		1.34	-0.19	-73.5	-290.	1.24	-0.12	-59.0	-303.	1.19	0.02	-50.9	-322.
2.5		2.94	3.10	-421.	-637.	2.60	2.68	-391.	-635.	2.33	2.41	-362.	-634.
1.2	148	1.33	-1.30	-30.7	-124.	1.22	-1.12	-23.4	-129.	1.11	-1.09	-12.1	-127.
1.7		1.93	0.34	-87.6	-181.	1.76	0.34	-80.3	-186.	1.66	0.44	-76.5	-192.
2.5		4.12	4.20	-293.	-386.	3.68	3.76	-282.	-388.	3.34	3.43	-271.	-387.
1.2	49	3.01	0.00	-61.7	-92.4	2.72	0.00	-58.9	-93.1	2.54	-0.09	-55.3	-91.1
1.7		3.92	1.95	-90.0	-121.	3.55	1.78	-87.6	-122.	3.34	1.73	-85.1	-121.
2.5		8.27	8.10	-224.	-255.	7.44	7.30	-221.	-255.	6.96	6.82	-217.	-253.

Table 6. Results from nozzle parameter study, variation with jet gas total temperature (AR=1, M=2.5, STP freestream conditions).

PR	T_{0j}	K_f	K_m	F_{ji}	F_{total}
49		8.27	8.10	-224.	-255.
148	300	4.12	4.20	-293.	-386.
340		2.94	3.10	-421.	-637.
49		8.34	8.17	-224.	-255.
148	1500	4.15	4.24	-294.	-388.
340		2.95	3.1	-421.	-636.
49		8.67	8.64	-234.	-265.
148	2700	4.43	4.68	-320.	-413.
340		3.18	3.50	-470..	-685.

Table 7. Results from nozzle parameter study, variation with altitude, (AR=2, M=2.5, T_{0j} =300 K).

PR	Altitude	K_f	K_m	F_{ji}	F_{total}
49		8.27	8.10	-224.	-255.
148	SL	4.12	4.20	-293.	-386.
340		2.94	3.10	-421.	-637.
63		6.34	6.24	-185.	-219.
189	2 km	3.31	3.38	-244.	-350.
434		2.43	2.50	-349.	-594.
189		3.51	3.50	-88.2	-123.
567	10 km	2.34	2.39	-142.	-249.
1305		1.94	1.96	-232.	-477.

Figure 9a–c shows the force amplification factor variation with Mach number and AR for the three pressure ratios. In all cases, K_f increases with Mach number and decreases with increasing PR. Generally, there is a small decrease in K_f with an increase in AR, with a larger effect at the higher Mach numbers. Figure 9d shows the variation of K_f with PR and AR at Mach 2.5, illustrating that the largest effect on K_f is PR.

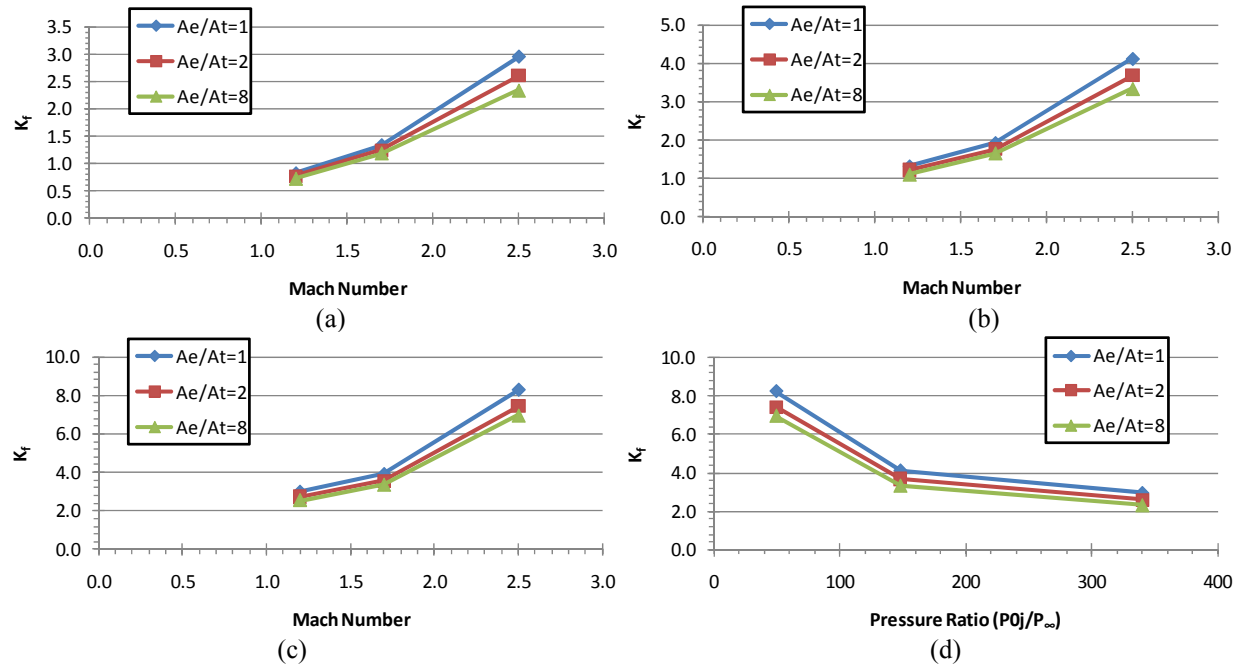


Figure 9. Force amplification factor variation with Mach number and AR for flat plate simulations, (a) PR=340, (b) PR=148, and (c) PR=49, and (d) variation with PR and AR at Mach 2.5.

Figure 10a shows that variation of K_f with PR and T_{0j} , indicating a negligible effect of the jet gas total temperature. Figure 10b shows the variation of K_f with PR and freestream altitude, which is primarily an extension of the pressure ratio due to the reduced freestream static pressure. This again shows that the pressure ratio is the dominant parameter of those investigate here. The reduction in K_f does appear to asymptote at very large PR.

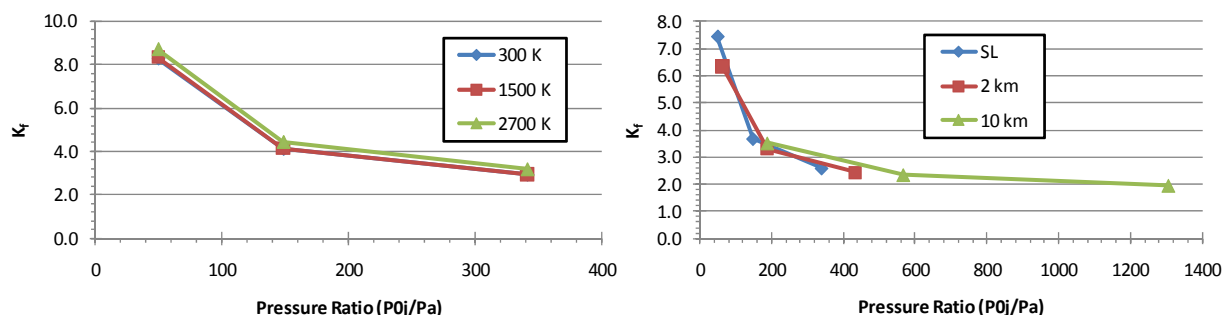


Figure 10. Force amplification factor variation with PR and (a) jet gas total temperature and (b) freestream conditions (altitude), at Mach 2.5.

B. Army-Navy Finner Test Case

Simulations were performed with the sonic nozzle shown in Fig. 5d located at the seven jet locations of Table 3 at Mach 1.5 and 2.5. Figure 11 shows the jet exit region for the jet in the F0 location at both Mach numbers. The jet exits the orifice at Mach 1 then accelerates to about Mach 10 within the barrel shock, which terminates with a Mach disk. There is a small subsonic region downstream of the Mach disk. The Mach disk is less pronounced at Mach 2.5. There is also a second high pressure region forward of the bow shock due to the λ -shock. The pressure in this region varies in intensity with Mach number and jet location, as observed in Fig. 12.

Figure 12 shows the resulting flowfield for all seven configurations, with the Mach 2.5 results on the left and the Mach 1.5 results on the right. The contours in Fig. 12 are the local pressure, normalized by the freestream pressure, P/P_∞ , (scale 0.5 to 2.0) on the projectile surfaces and Mach number (scale 0 to 10) on the symmetry plane. The resulting flowfield is typical of what is observed in the literature^{5,6}: a high pressure region behind the bow shock ahead of the jet and an extended low pressure region behind the jet. The high pressure from the bow shock wraps around the projectile as does a second low pressure region, due to horseshoe vortices emanating from the boundary layer separation region between the jet bow shock and the jet exit (see Fig. 11). A shock appears to emanate from the Mach disk at the end of the barrel shock and impacts the projectile and fins—depending on jet location. The higher dynamic pressure of the Mach 2.5 flow results in both a greater turning of the jet plume, and a smaller jet plume.

Figure 13 shows vorticity contours on axial planes from the jet exit to the rear of the projectile or beyond for both Mach numbers. The main wake vortices (Fig. 1) can clearly be seen forming shortly aft of the jet exit. The main axial jet plume flow is directly above these vortices. The horseshoe vortices can also be observed on the lower side of the projectile body, nearly in line with the lower tail fins. All vortices are more compact and have a higher intensity in the higher freestream flow.

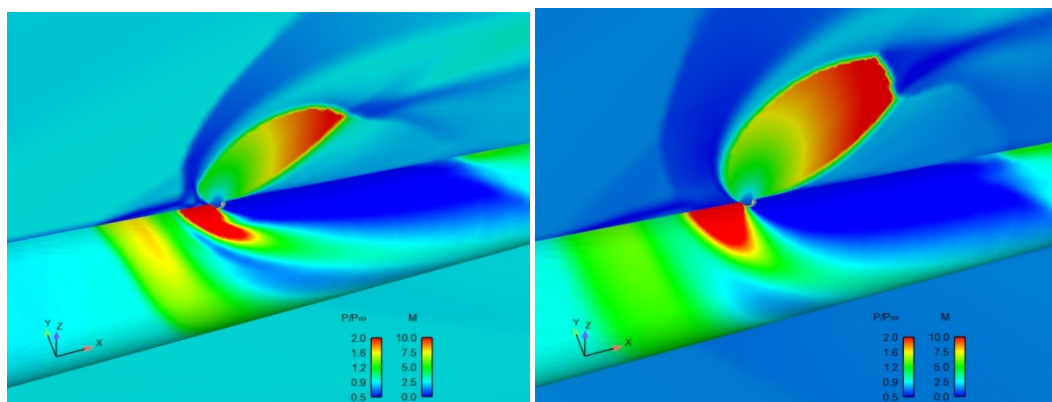


Figure 11. Normalized pressure on projectile surfaces and Mach number on symmetry plane (Mach 2.5 left, Mach 1.5 right) in region near jet (jet location F0).

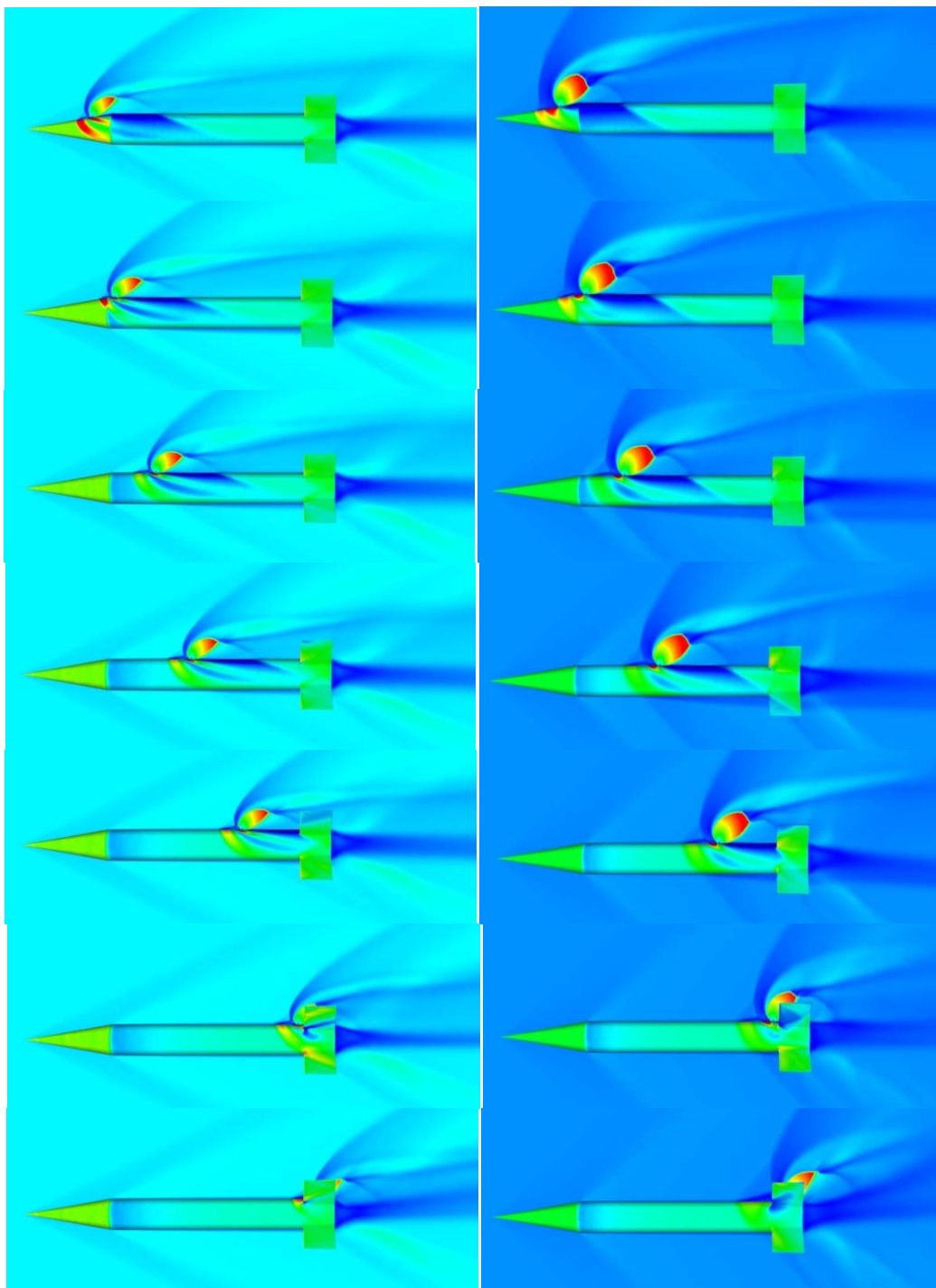


Figure 12. Normalized pressure (scale: 0.5–2.0) on projectile surfaces and Mach number (scale: 0–10) on symmetry plane (Mach 2.5 left, Mach 1.5 right) for jet locations (from top) F3, F2, F1, F0, R1, R2, and R3.

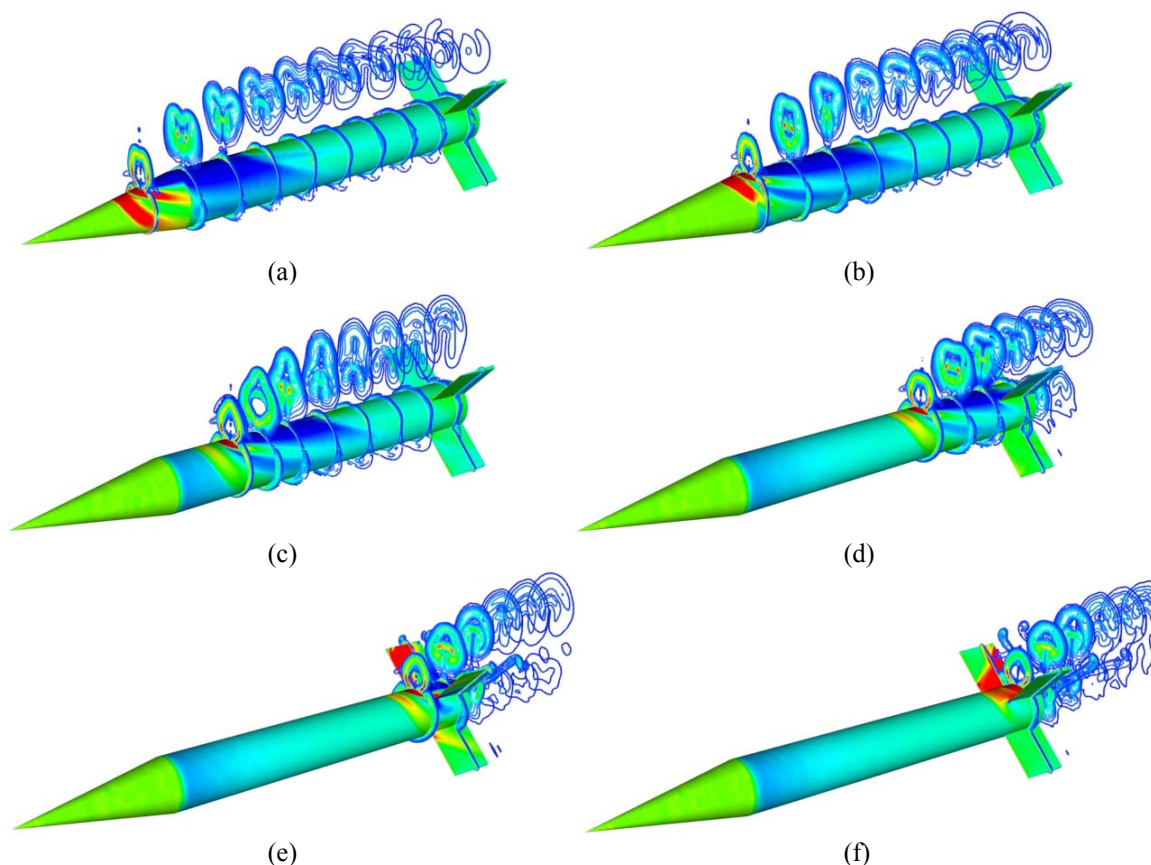


Figure 13. Normalized pressure (scale: 0.5–2.0) on projectile surfaces and vorticity contours (scale: 0–500,000) on axial plane locations (a) F3, (b) F2, (c) F1, (d) R1, (e) R2, and (f) R3 at Mach 2.5.

From Figs. 12 and 13, one may assume that locating the jet toward the aft of the projectile will minimize the JI effect, primarily due to the limited area for the flow features aft of the jet exit to act. In fact, the JI force changes from one opposing the jet thrust to one acting in conjunction with the jet thrust as the jet exit is located closer to the tail fins. This is due to a combination of a minimized region of low pressure aft of the jet, action of the high pressure region forward of the jet, and interaction of the jet (increased local pressure) on the two top tail fins. These effects are illustrated in Figure 14, which shows the JI force and moment distribution along the projectile body. The profile of the projectile (minus the tail fins) is also shown in the plots. The tail fins leading edge is at 0.27 m. For all locations except the two aft R2 and R3 locations, the JI force is positive (up), which is opposite the jet thrust. At the R2 and R3 locations a JI force about 3 times in magnitude of that observed at the other locations results in the

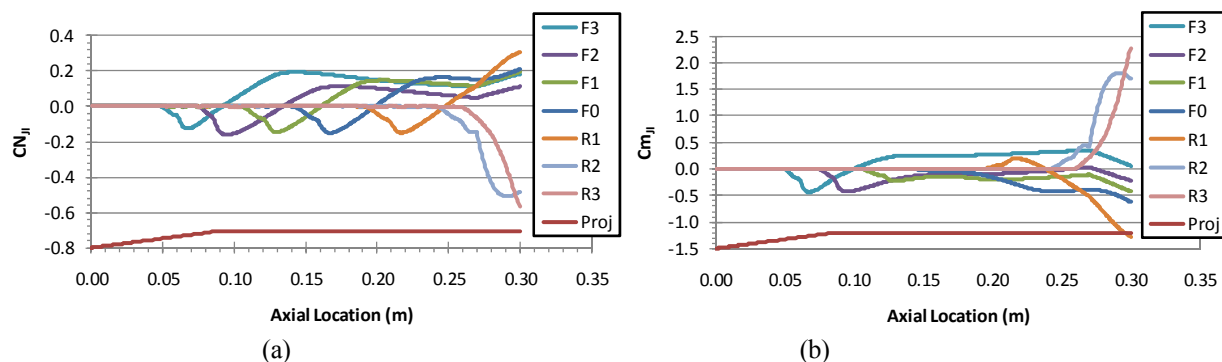


Figure 14. JI (a) force and (b) moment distributions along projectile body (Mach 2.5, PR=340).

same direction as the jet thrust and will lead to an amplification of the jet thrust. A similar trend is observed in the JI moments (Figure 14b), however, for the overall effect on the moment amplification factor, the moment due to the jet thrust needs to be included and is discussed below.

The force distributions provide a cumulative integrated effect of the JI. The localized action of the JI effects are shown in Fig. 15, which shows the local normalized pressure on the upper and lower surfaces of the projectile along the symmetry plane. A constant pressure of about 1.4 is observed along the conical nose, followed by an expansion to about 0.75 as the flow turns to flow along the cylindrical section of the body. These values are the same on the upper and lower surfaces since the projectile is at zero angle of attack. On the upper surface, the pressure ahead of the jet ranges from about 1.5 to 2.9, while the pressure behind the jet minimizes at about 0.2, then increases to about 1.3 before equilibrating to the no-jet case pressure if the jet is far enough forward. On the lower surface there is less of an effect, with the pressure only affected behind the jet and increasing to about 1.0 to 1.25.

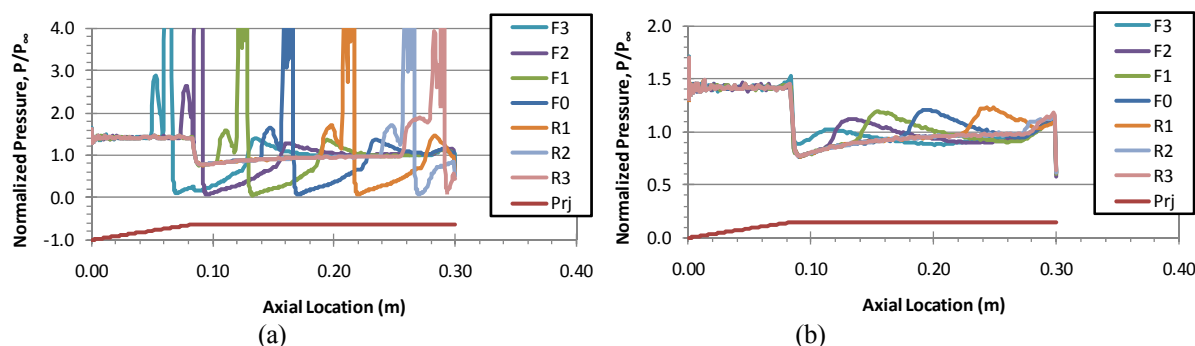


Figure 15. Normalized pressure along projectile (a) upper and (b) lower surfaces (Mach 2.5, PR=340).

The force and moment amplification factors, K_f and K_m , are good indicators of the overall effect of the JI on the reaction jet system (Fig. 16). Here it is observed that the jet thrust force is attenuated about 15-45% at Mach 2.5 and about 25-75% at Mach 1.5 for the forward five jet locations. The jet thrust force is amplified by 70-80% at Mach 2.5 and 6-80% at Mach 1.5 for the two rear locations. In general, the moment due to the jet thrust was near neutral or amplified at most jet locations. However, at the R1 location, the moment amplification factor was negative at both Mach numbers, indicating an induced moment that acts to oppose the moment due to the jet thrust.

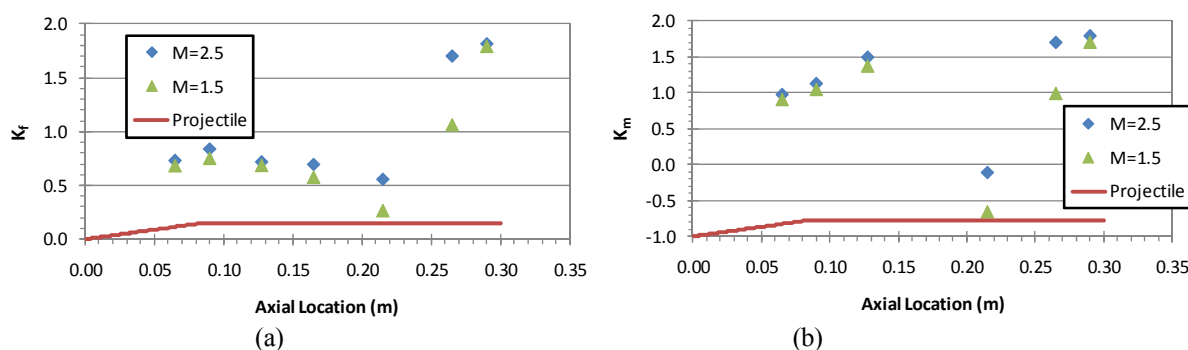


Figure 16. (a) Force and (b) moment amplification factors as function of jet location (PR=340).

Figure 17 shows the JI, jet, and total force and moment coefficients versus jet location for both Mach numbers. The jet force is constant, since the pressure ratio is constant, while the moment due to the jet force varies linearly with the jet location. The total pitching moment $C_{m_{total}}$, and pitching moment due to JI, $C_{m_{ji}}$, are the same at location F0, since the moment due to the jet thrust is zero about the c.g. It is observed that the pitching moment due to the jet thrust dominates as the jet is located farther forward and $C_{m_{ji}}$ approaches zero.

Figure 18 shows the same data in the form of the force center of pressure with respect to the c.g., defined in Eq. (4). For both Mach numbers, the resultant force center of pressure (RFCP, "total" in Fig. 18) varies fairly linearly with jet location when located from the c.g. and forward. In all cases, the RFCP is either forward of the jet

location or very close to it—as when located near the tail (last two locations in Fig. 18). At the R1 location at Mach 1.5, the RFCP is well forward (125 mm) of the c.g. At this location, about 2 cal. from leading edge of the fins, Figs. 14 and 17 show that there is a large positive (upward) JI force acting at 113 mm aft the c.g., which is just in front of the fins. This results in a negative (nose down) total pitching moment, even though the jet is located to the rear of the c.g. This results in the negative K_m values shown in Fig. 16. A similar, though much smaller, effect is observed at Mach 2.5 at the R1 location.

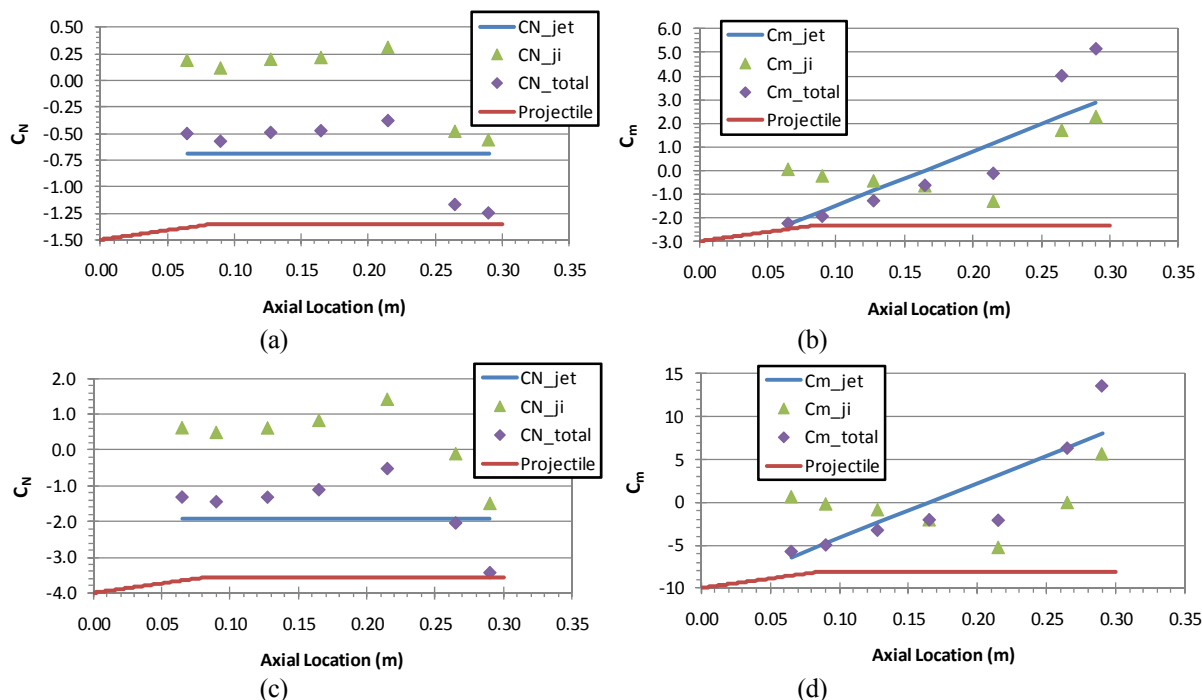


Figure 17. (a, c) Force and (b, d) moment coefficients as function of jet location (PR=340) at (a, b) Mach 2.5 and (c, d) Mach 1.5.

Figures 17 and 18 also show that $C_{m_{total}}$ is not zero when the jet is located at the c.g. (F0 location). $C_{m_{total}}$ is -0.63 at Mach 2.5 and -2.1 at Mach 1.5 (nose down), with RFCPs of 39.3 and 56.3 mm forward of the c.g., respectively. This is expected, as the JI results in a high pressure forward and a low pressure rearward of the c.g.

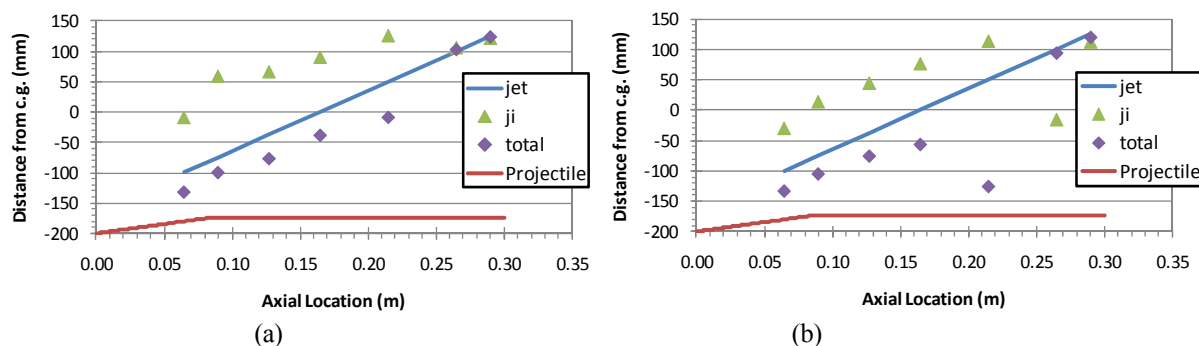


Figure 18. Force center of pressure as function of jet location (PR=340), (a) Mach 2.5 and (b) Mach 1.5.

Further analysis of these data are planned to evaluate the contribution of the JI effects on the tail. However, a series of simulations were performed on the ANF body alone configuration for the same jet locations and same conditions (PR=340, Mach 1.5 and 2.5). Figure 19 shows a comparison of the force and moment amplification

factors for the body-tail and body alone configurations. For both Mach numbers, there is less attenuation of the jet thrust and resulting moments at the first five locations. As expected, the presence of the tail fins has a more pronounced effect on the JI as the jet is located farther rearward. At the rearward locations, there is less amplification of the jet force and moment. There is also a Mach number effect at the rearward locations, most notably at the R1 and R2 locations. The latter is likely due to the differing shock angles (see Fig. 12) and their impact on the tail fins, as the body alone amplification factors are similar (near 1.0) for both Mach numbers. Locating the jet closer to the nose minimizes the JI effect on tail fins.

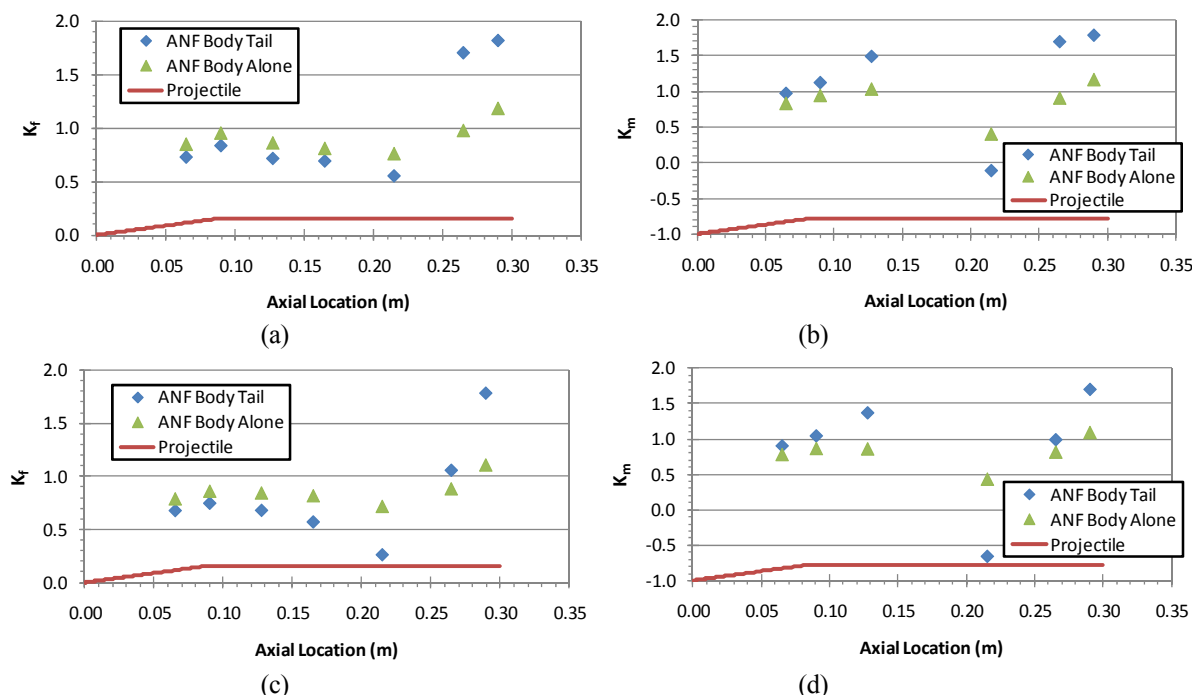


Figure 19. (a, c) Force and (b, d) moment amplification factors as function of jet location (PR=340) at (a, b) Mach 2.5 and (c, d) Mach 1.5.

In addition to the high pressure ratio jet (PR=340), simulations were also performed at two lower pressure ratios of 148 and 49, representative of lower energy squibs and pressurized gas used in wind tunnel experiments, respectively. Figure 20 shows a comparison of the results for the three jet pressure ratios for the sonic jet (AR=1) at Mach 1.5 and 2.5. In general, at the forward four locations, more attenuation of the jet force is observed as the jet pressure ratio decreases. The trend reverses at some locations rearward of the c.g.: at Mach 2.5 (Fig. 20a), at the R1 and R2 locations, and at Mach 1.5 (Fig. 20b) at the R2 and R3 locations. The force amplification factor is relatively independent of PR at the R3 and R1 locations at Mach 2.5 and 1.5, respectively. This again shows the strong coupling of JI and the tail fins when the jet is located close to the tail fins.

In addition to the sonic nozzle, nozzles with area ratios of 2 and 8 were also investigated. Force amplification factors for all three area ratios at Mach 2.5 are shown in Fig. 21a–c, respectively, for the three jet locations F1, F0, and R3. We see that the jet nozzle area ratio has little effect on the jet force amplification factor at the F1 and F0 jet locations. However, there is a small decreasing trend of the force amplification factor with increasing nozzle area ratio at the R3 jet location, likely due to a different size of the jet plume as the nozzle area changes.

These results confirm that the choice of location for a reaction jet can have a significant effect on the resulting aerodynamic forces and moments. In practical situations the designer may be limited to where the jet can be located due to other considerations for payload, GN&C components, etc. One may consider that locating the reaction jet at the rear, near or between fins as optimal. However, flight dynamics studies indicate that the aft end of a fin-stabilized munition may be the least optimum location for a control system (the nose being optimum).^{29,30} A flight dynamics analysis of the system is needed to determine the overall effects on the flight of the projectile.

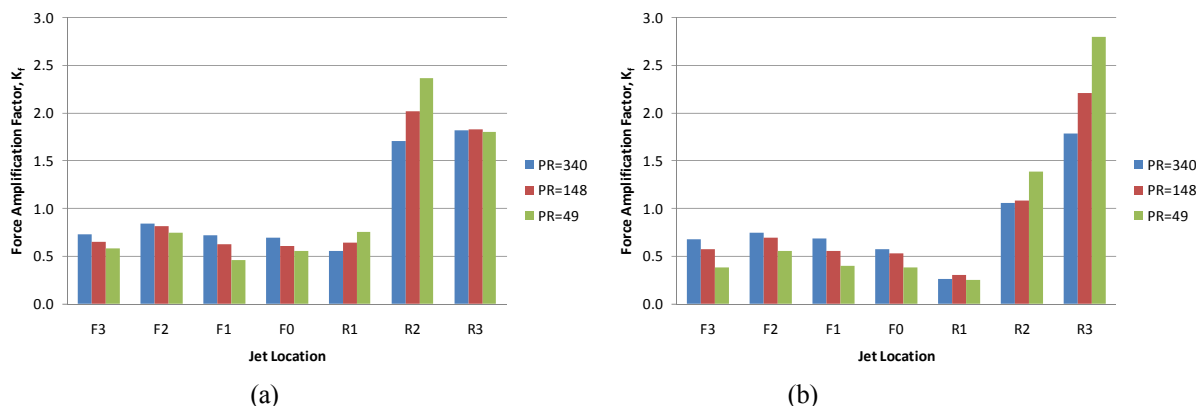


Figure 20. Force amplification factor as function of jet location and PR at Mach (a) 2.5 and (b) 1.5 (AR=1).

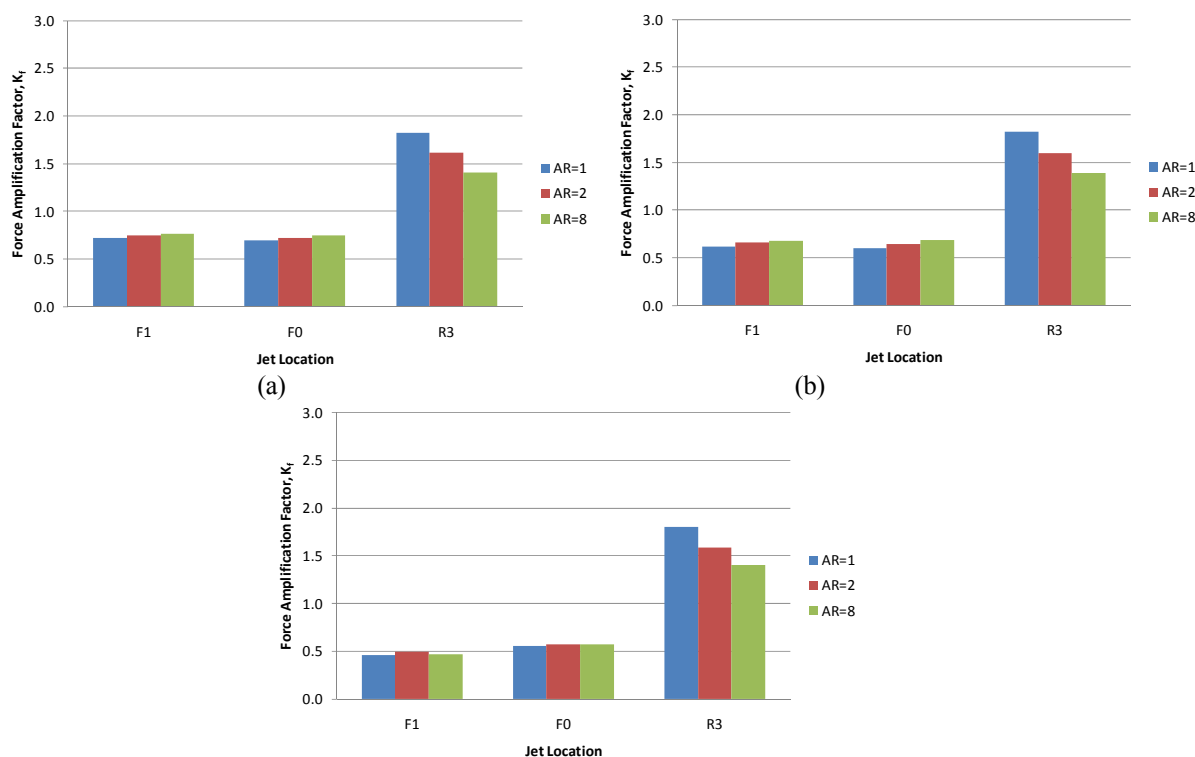


Figure 21. Force amplification factor as function of jet location and AR (a) PR=340, (b) PR=148, and (c) PR=49 (Mach 2.5).

IV. Summary and Conclusions

The jet interaction effects resulting from a supersonic jet venting into a supersonic crossflow were investigated for the case of a flat plate and a generic fin-stabilized projectile. Mesh generation and turbulence model variation studies were performed with the flat plate configuration. Simulations were performed with a sonic nozzle (jet exit to throat area ratio, AR, of one) and supersonic nozzles with AR=2 and AR=8. Simulations were performed at three supersonic freestream Mach numbers and several jet total to freestream static pressure ratios (PR). Some conclusions that can be drawn from these flat plate results are as follows.

- The jet interaction (JI), as determined from the jet amplification factor, K_f , was most dependent on PR and the freestream Mach number.
- K_f was found to increase with Mach number and decrease with increasing PR.
- There was only a small variation of K_f with AR.
- There was very little variation of K_f with the jet gas total temperature, T_{0j} .
- There was a strong decrease in K_f with increasing altitude, primarily due to the increase in PR as the freestream static pressure decreases with altitude.
- The data show that the jet force is usually amplified ($K_f > 1$) for jets issuing from a flat plate, into a supersonic freestream. K_f does decrease as the Mach number is reduced, eventually leading to attenuation of the jet force.

For the Army-Navy Finner (ANF) projectile, simulations were performed with a sonic nozzle located on the top surface of the projectile, at seven positions along the projectile axis. Some conclusions drawn from the ANF results are as follows.

- Locating the jet near the tail fins can minimize the traditional JI effects due to interactions in the jet wake, however, the interaction of the near-jet flowfield with the fins must be taken into account. There is generally an amplification of the jet force when the jet is located very near the tail fins.
- The jet thrust force was attenuated about 15-45% at Mach 2.5 and about 25-75% at Mach 1.5 for the forward five jet locations. The jet thrust force was amplified by 70-80% at Mach 2.5 and 6-80% at Mach 1.5 for the two rear locations.
- In general, the moment due to the jet thrust was near neutral or amplified at most jet locations (see Table 3). However, at the R1 location, the moment amplification factor was negative at both Mach numbers, indicating an induced moment that acts to oppose the moment due to the jet thrust.
- In all cases, the resultant force center of pressure (RFCP) was either forward of the jet location or very close to it, e.g., when the jet was located near the tail.
- At the R1 location a negative (nose down) resultant pitching moment is observed, even though the jet is located to the rear of the c.g.
- For the jet located at the c.g. (F0 location), the resultant pitching moment is not zero due to the JI force, but one that induces a negative (nose down) pitching moments.
- Comparisons of the ANF results with those from a body alone (no tail fins) configuration show that the jet flow interaction with the tail are minimal when the jet is located toward the nose of the projectile.
- At the forward four locations, more attenuation (decreasing K_f) of the jet force is observed as PR decreases, which is opposite that found for the flat plate. At the rearward locations, the trend is the same as that for the flat plate, including a general amplification of the jet force.
- The jet area ratio, AR, was found to have a small effect on K_f at the forward locations. At the R3 location, there was a small decreasing trend of K_f with increasing AR.

Some general conclusions are,

- The features of the jet interaction flowfield compared well with those presented and described in the archival literature.
- The choice of turbulence model can affect accurate prediction of the features of the interaction flowfield. In the flat plate configuration, differences of up to 13% and 15% were observed in the force amplification factor and JI force, respectively.

These results confirm that the choice of location for a reaction jet can have a significant effect on the resulting aerodynamic forces and moments. Future investigation of the ANF configuration in a supersonic crossflow is planned; to include a higher supersonic Mach number and also to investigate the effects of projectile angle of attack on the jet interaction effects.

Acknowledgments

This work was supported in part by grants of high-performance computing time from the U.S. Department of Defense (DOD) High Performance Computing Modernization program at the Army Research Laboratory DOD Supercomputing Resource Center (DSRC), Aberdeen Proving Ground, MD, and the Air Force Research Laboratory DSRC, Wright-Patterson Air Force Base, OH.

References

- ¹Margason, R. J., "Fifty Years of Jet in Cross Flow Research," AGARD, 72nd Fluid Dynamics Panel Meeting, Paper 1, 1993.
- ²Spaid, F. W., and Cassel, L. A., "Aerodynamics Interference Induced by Reaction Controls," AGARDograph No. 173, Dec. 1973.
- ³Champigny, P., and Lacau, R. G., "Lateral Jet Control for Tactical Missiles," *Special Course on Missile Aerodynamics*, AGARD-R-804, Paper 3, 1994.
- ⁴Cassel, L. A., "Applying Jet Interaction Technology," *AIAA J. of Spacecraft and Rockets*, Vol. 40, No. 4, 2003, pp. 523–537.
- ⁵Dickmann, D. A., and Lu, F. K., "Shock/Boundary-Layer Interaction Effects on Transverse Jets in Crossflow Over a Flat Plate," *AIAA J. of Spacecraft and Rockets*, Vol. 46, No. 6, 2009, pp. 1132–1141.
- ⁶Dickmann, D. A., and Lu, F. K., "Shock/Boundary Layer Interaction Effects of Transverse Jets in Crossflow Over a Body of Revolution," AIAA-2009-4146, June 2009.
- ⁷Kovar, A., and Schulein, E., "Comparison of experimental and numerical investigation on a jet in a supersonic cross-flow," *The Aeronautical Journal*, June 2006, pp. 353–360.
- ⁸Gnemmi, P., Adeli, R., and Longo, J., "Computational Comparisons of the Interaction of a Lateral Jet on a Supersonic Generic Missile," AIAA-2008-6883, August 2008.
- ⁹Gnemmi, P., and Schafer, H. J., "Experimental and Numerical Investigations of a Transverse Jet Interaction on a Missile Body," AIAA-2005-0052, January 2005.
- ¹⁰Graham, M. J., and Weinacht, P., "Numerical Investigation of Supersonic Jet Interaction for Axisymmetric Bodies," *Journal of Spacecraft and Rockets*, Vol. 37, No. 7, 2000, pp. 675–683.
- ¹¹Graham, M. J., Weinacht, P., and Brandeis, J., "Numerical Investigation of Supersonic Jet Interaction for Finned Bodies," *Journal of Spacecraft and Rockets*, Vol. 39, No. 3, 2002, pp. 376–383.
- ¹²Beresh, S. J., Henfling, J. F., Erven, R. J., and Spillers, R. W., "Penetration of a Transverse Supersonic Jet into a Subsonic Compressible Crossflow," *AIAA Journal*, Vol. 43, No. 2, 2005, pp. 379–389.
- ¹³Beresh, S. J., Henfling, J. F., Erven, R. J., and Spillers, R. W., "Turbulent Characteristics of a Transverse Supersonic Jet into a Subsonic Compressible Crossflow," *AIAA Journal*, Vol. 43, No. 11, 2005, pp. 2385–2394.
- ¹⁴Beresh, S. J., Henfling, J. F., Erven, R. J., and Spillers, R. W., "Crossplane Velocimetry of a Transverse Supersonic Jet in a Transonic Crossflow," *AIAA Journal*, Vol. 44, No. 12, 2006, pp. 3051–3061.
- ¹⁵Beresh, S. J., Heineck, J. T., Walker, S. M., Schairer, E. T., and Yaste, D. M., "Stereoscopic PIV for Jet/Fin Interaction Measurements on a Full-Scale Flight Vehicle," AIAA-2005-0442, January 2005.
- ¹⁶Beresh, S. J., "Aerodynamic Origin of Jet/Fin Interaction on a Full-Scale Flight Vehicle Configuration," AIAA-2007-0673, January 2007.
- ¹⁷Dowdy, M. W., and Newton, J. F., "Investigation of Liquid and Gaseous Secondary Injection Phenomena on a Flat Plate with $M = 2.01$ and $M = 4.54$," JPL-TR-32-542, Dec. 1963.
- ¹⁸Metacomp Technologies, Inc., "MIME User Manual," Agoura Hills, CA, 2008.
- ¹⁹Dupuis, A. D., "Aeroballistic Range and Wind Tunnel Tests of the Basic Finner Reference Projectile from Subsonic to High Supersonic Velocities," TM-2002-137, Defence R&D Canada Valcartier, Canada, Oct. 2002.
- ²⁰Dupuis, A. D., and Hathaway, W., "Aeroballistic Range Tests of the Basic Finner Reference Projectile at Supersonic Velocities," DREV-TM-9703, Defence Research Establishment, Valcartier, Canada, Aug 1997.
- ²¹Metacomp Technologies, Inc., "CFD ++ User Manual," Agoura Hills, CA, 2010.
- ²²Menter, F. R., "Two-Equation Eddy-Viscosity Turbulence Models For Engineering Applications," *AIAA Journal*, Vol 32, No. 8, 1994, pp. 1598–1605.
- ²³Hirsch, C., "Lessons Learned from the First AIAA-SWBLI Workshop CFD Simulations of Two Test Cases," AIAA-2010-4824, June 2010.
- ²⁴Spalart, P R, Allmaras, S R, "A One-Equation Turbulence Model for Aerodynamic Flows," *Recherche Aerospatiale*, No 1, pp 5–21, 1994.
- ²⁵Chien, K-Y, "Predictions of Channel and Boundary Layer Flows with a Low-Reynolds-Number Turbulence Model," *AIAA Journal*, Vol 20, No 1, 1982.
- ²⁶Goldberg U, Batten, P, Palaniswamy, S, Chakravarthy, S, Peroomian, O, "Hypersonic Flow Predictions Using Linear and Nonlinear Turbulence Closures," *AIAA Journal of Aircraft* Vol 37, No 4, July/August 2000.
- ²⁷Goldberg U, Peroomian, O, Chakravarthy, S, "Application Of The $k-\epsilon-R$ Turbulence Model To Wall-Bounded Compressive Flows," AIAA 98-0323, January 1998.
- ²⁸Batten P, Craft T J, Leschziner M A, and Loyau H, "Reynolds-stress-transport modeling for compressible aerodynamics applications," *AIAA Journal*, Vol 37, No 7, July 1999.
- ²⁹Fresconi, F., and Plostins, P., "Control Mechanism Strategies for Spin-Stabilized Projectiles," *J. Aerospace Engineering*, Vol 224, No. G9, pp. 979–991, 2010.
- ³⁰Ollerenshaw, D., and Costello, M., "Simplified Projectile Swerve Solution for General Control Inputs," *AIAA J. of Guidance, Control, and Dynamics*, Vol. 31, No. 5, 2008, pp. 1259–1265.